LEGIBILITY NOTICE

A major purpose of the Technical Information Center is to provide the broadest dissemination possible of information contained in DOE's Research and Development Reports to business, industry, the academic community, and federal, state and local governments.

Although a small portion of this report is not reproducible, it is being made available to expedite the availability of information on the research discussed herein.

LA-UR -88-376

CONF-8802102--4

Los Alamos National Laboratory is operated by the University of California for the United States Department of Energy under contract W-7405-ENG-36.

TITLE: RECENT RESULTS IN THE DEVELOPMENT OF A GLOBAL MEDIUM-ENERGY NUCLEON-NUCLEUS OPTICAL-MODEL POTENTIAL

LA-UR--88-376

DE88 006474

AUTHOR(S): David G. Madland, T-2

SUBMITTED TO The OECD/NEANDC Specialists' Meeting, Semmering, Austria, February 10-12, 1988.

DISCLAIMER

MASTER

Los Alamos National Laboratory
Los Alamos, New Mexico 87545

RECENT RESULTS IN THE DEVELOPMENT OF A GLOBAL MEDIUM-ENERGY NUCLEON-NUCLEUS OPTICAL-MODEL POTENTIAL

D. G. Madland
Theoretical Division, Los Alamos National Laboratory
Los Alamos, New Mexico 87545 USA

ABSTRACT

Initial results are presented for the determination of a global medium-energy nucleon-nucleus phenomenological optical-model potential using a relativistic Schrödinger representation. The starting point for this work is the global phenomenological optical-model potential of Schwandt *et al.*, which is based on measured elastic scattering cross sections and analyzing powers for polarized protons ranging from 80 to 180 MeV. This potential is optimally modified to reproduce experimental proton reaction cross sections as a function of energy, while allowing only minimal deterioration in the fits to the elastic cross sections and analyzing powers. Further modifications in the absorptive potential were found necessary to extrapolate the modified potential to higher energies. The final potential is converted to a neutron-nucleus potential by use of standard Lane model assumptions and by accounting approximately for the Coulomb correction. Comparisons of measured and calculated proton reaction and neutron total cross sections are presented for ^{27}Al, ^{56}Fe, and ^{208}Pb. Medium-energy optical-model potentials for complex projectiles are briefly discussed in an appendix.

INTRODUCTION

Realistic calculations of specific medium-energy proton- or neutron-induced reactions that take into account distortion effects and total flux conservation require an optical-model potential that satisfactorily reproduces the elastic scattering and integrated scattering observables at these energies. In particular, the observed elastic differential cross section $\sigma(\theta)$ and analyzing power $A_y(\theta)$ should be well reproduced in order that distortion effects are correctly described, and the observed proton total reaction cross section σ_R or neutron total cross section σ_T should be well reproduced in order that the calculated specific reactions all sum to the correct physical value. In this work the status of a global phenomenological nucleon-nucleus optical-model potential for medium-energy scattering that is being developed[1,2] is presented. This potential primarily reproduces the integrated scattering observables and secondarily, the elastic scattering observables. Described here is how the potential is obtained and how its predictions compare with the measured observables.

METHOD

The starting point of this work is the global phenomenological proton optical-model potential of Schwandt *et al.*[3] This potential is based upon experimental elastic scattering and analyzing power angular distributions for target masses A and incident proton energies E_p in the ranges

$$24 \le A \le 208, \text{ and}$$
$$80 \text{ MeV} \le E_p \le 180 \text{ MeV}, \tag{1}$$

respectively. The data were analyzed in the framework of a relativistic Schrödinger-type wave equation[4] generated by appropriate reduction of the Dirac equation for a massive, energetic fermion moving in a localized, central potential V(r). If the potential V(r) is chosen to be the fourth (time-like) component of Lorentz vector potential, the reduced two-body problem with relativistic projectile mass and non-relativistic target mass then leads to a relativistic radial wave equation for the ℓ'th partial wave that is of the same form as for the conventional non-relativistic Schrödinger equation, namely,

$$\left\{ \frac{d^2}{d\rho^2} + \left[1 - \frac{\gamma V(\rho)}{T_c} - \frac{\ell(\ell+1)}{\rho^2} \right] \right\} F_L(\rho) = 0 . \tag{2}$$

In this equation, $\rho = kr$ where k is the relativistic wave number, T_c is the total center-of-mass kinetic energy, and γ is a factor by which the potential is renormalized in the relativistic calculation,

$$\gamma = 1 + T_c/(T_c + 2m) . \tag{3}$$

Using this formalism, an energy-dependent complex potential of Woods-Saxon form was assumed and best-fit parameters were obtained for each individual experimental data set by performing least-squares adjustments. The resulting sets of parameters were then examined for simple dependencies with respect to the incident proton energy, the target mass number, and the target asymmetry parameter (N-Z)/A. In this way, Schwandt *et al.*[3] obtained the following global phenomenological proton potential:

$$V_R = 105.5(1 - 0.1625 \ln E_p) + 16.5 (N-Z)/A , \tag{4}$$

$$r_R = 1.125 + E_p/10^3 \text{ , } E_p \le 130 \text{ MeV}$$
$$= 1.255, \qquad E_p > 130 \text{ MeV} \qquad (5)$$

$$a_R = 0.675 + 3.1\, E_p/10^4 \text{ ,} \qquad (6)$$

$$W_V = 6.6 + 2.73\,(E_p - 80)/10^2 + 3.87\,(E_p - 80)^3/10^6 \text{ ,} \qquad (7)$$

$$r_I = 1.65 - 2.4\, E_p/10^3 \text{ ,} \qquad (8)$$

$$a_I = 0.32 + 2.5\, E_p/10^3 \text{ ,} \qquad (9)$$

$$V_{SO} = 19.0(1 - 0.166 \ln E_p) - 3.75\,(N\text{-}Z)/A \text{ ,} \qquad (10)$$

$$W_{SO} = 7.5(1 - 0.248 \ln E_p) \text{ ,} \qquad (11)$$

$$r_{VSO} = 0.920 + 0.0305\, A^{1/3} \text{ ,} \qquad (12)$$

$$a_{VSO} = 0.768 - 0.0012\, E_p \text{ , } E_p \le 140 \text{ MeV}$$
$$= 0.60 \text{ , } \qquad E_p > 140 \text{ MeV} \qquad (13)$$

$$r_{WSO} = 0.877 + 0.0360 A^{1/3} \text{ , and} \qquad (14)$$

$$a_{WSO} = 0.62 \text{ ,} \qquad (15)$$

where the units are MeV and fermis. The only deviations found in Eqs. (4)-(15) were that (a) $r_{VSO} = 0.98$ and $r_{WSO} = 0.96$, for ^{24}Mg and ^{28}Si at 135 MeV, and (b) the transition point in r_R, Eq. (5), for Ca occurs at 180 MeV instead of 130 MeV.

Using this potential as a starting point, the goal is defined as a global phenomenological nucleon-nucleus optical-model potential valid for target masses and incident nucleon energies in the ranges

$$24 \le A \le 208, \text{ and}$$
$$50 \text{ MeV} \le E_p, E_n \le 400 \text{ MeV} \text{ ,} \qquad (16)$$

respectively. Comparing Eqs. (1) and (16), one sees that there are two tasks. The first is to extend the energy range of the proton potential downwards to 50 MeV and upwards to 400 MeV. The second is to attempt to transform the extended proton potential to a neutron potential valid for the same energy range.

The method used consists of the following: *Only* the parameters of the proton central absorptive potential (W_V, r_I, a_I) are adjusted to optimally reproduce the experimental proton total reaction cross section σ_R in the extended energy range. All other parameters remain at their original values. In particular, the spin-dependent absorptive potential (W_{SO}, r_{WSO}, a_{WSO}) remains

unchanged due to the fact that, at this stage, experimental spin-dependent observables have not yet been included from the extended energy range in the analysis. The adjustments to the parameters of the absorptive potential are performed allowing only *small* changes in the calculated elastic scattering observables. Assuming a satisfactory proton potential is obtained with this method, the transformation to the corresponding neutron potential is made by using a simple Lane model, namely,

$$(N\text{-}Z/A \rightarrow -(N\text{-}Z)/A \ , \tag{17}$$

wherever this factor appears [in V_R, Eq. (4), and in V_{SO}, Eq. (10)], and by using a simple Coulomb correction[5] in the real central potential, namely,

$$V_{CORR} = 0.4Z/A^{1/3} \ . \tag{18}$$

Note that no Coulomb correction explicitly appears in the real central part of the original potential, Eq. (4). Thus, to obtain the neutron potential, one assumes that this correction is present *implicitly* in the real central part of the proton potential so that *subtraction* of Eq. (18) completes the transformation.

All of the calculations reported in this work have been performed using the optical-model code [6] SNOOPY8 with relativistic wave equation (and relativistic kinematics) given by Eq. (2). A measure of the influence of relativistic effects is given in Figs. 1 and 2 where the calculated proton total reaction cross section and neutron total cross section are shown, respectively, as a function of projectile energy for three relativity options, using fixed parameter sets for protons and for neutrons. Clearly, for energies above 50 MeV, relativistic effects cannot be ignored where high accuracy is required. The magnitudes of the differences between the fully relativistic Schrödinger and nonrelativistic Schrödinger representations are 2.2% at 50 MeV, 4.6% at 100 MeV, and 10.5% at 400 MeV, for the proton reaction cross section, and are 1.3% at 50 MeV, 7.0% at 100 MeV, and 14.7% at 400 MeV, for the neutron total cross section.

Preliminary results have been obtained by considering the target nuclei ^{27}Al, ^{56}Fe, and ^{208}Pb, together with corresponding experimental proton total reaction cross sections and neutron total cross sections for the energy range given by Eq. (16). It was observed that the original proton potential of Schwandt *et al.*[3] predicts a total reaction cross section σ_R that increases strongly with increasing incident energy as one approaches the upper end of the range of validity for the model, 180 MeV, and in fact, diverges as the energy is increased further (beyond the range of the potential). The source of this divergence is the strong energy dependence chosen for the strength W_V of the central absorptive potential, namely, a third-order polynomial in the incident energy, as given in Eq. (7).

This problem is addressed by dividing the modified potential into two regions: a lower energy region in which no divergence occurs in σ_R and an upper energy region where the divergence in σ_R begins and grows with increasing energy. The form of W_V is then changed in the upper region so as to remove the divergence. An energy grid of 31 points was chosen to span the range given by Eq. (16), and a number of survey calculations were performed to determine the dividing point between the two regions. In this way, the value 140 MeV was determined. Thus, the two regions of the modified potential are defined as follows:

$$\begin{aligned} &\text{Region I:} \quad 50 \text{ MeV} \le E_p, E_n \le 140 \text{ MeV, and} \\ &\text{Region II:} \quad 140 \text{ MeV} < E_p, E_n \le 400 \text{ MeV.} \end{aligned} \tag{19}$$

A study was then performed using the same energy grid, in which various forms of the absorptive potential were tested and optimized with respect to reproduction of the experimental proton total reaction cross section, while minimizing the deviations from the elastic differential cross sections and analyzing powers calculated with the original potential (the approximation has been made here that these are identical to the experimental values). This study, for protons incident on ^{27}Al, ^{56}Fe, and ^{208}Pb, lead to the following adjustments in the central absorptive part of the original potential of Schwandt *et al.*[3]:

Region I: W_V is unchanged.

r_I is unchanged, and

$$a_I = 0.27 + 2.5\ E/10^3. \quad (20)$$

Region II: $$W_V = 7.314 + 0.0462E, \quad (21)$$

$$r_I = 1.17, \text{ and} \quad (22)$$

$$a_I = 0.59 \text{ for } ^{27}\text{Al}$$
$$= 0.66 \text{ for } ^{56}\text{Fe} \quad (23)$$
$$= 0.79 \text{ for } ^{208}\text{Pb}\ .$$

In Eqs. (20) and (21), E is either the incident proton energy E_p or the incident neutron energy E_n. The original proton potential of Schwandt et al.[3], Eqs. (4)-(15, together with the adjustments given by Eqs. (20)-(23), define the modified proton potential for the energy range given by Eq. (16). Similarly, the modified neutron potential for the same energy range is given by the identical equations together with the transformation given by Eqs. (17) and (18). It is noted here that neutron scattering observables were *not* used to determine the adjustments, Eqs. (20)-(23). Thus, a good test of the assumed transformation to neutron scattering, given by Eqs. (17) and (18), will be obtained in subsequent comparisons to the neutron measurements (next section). It is also noted here that the modified potential is *discontinuous* across the 140-MeV boundary, for both proton and neutron scattering. This is a serious drawback of the modified potential and it will have to be corrected in the final version. Nevertheless, even in its present form, the discontinuous potential does *not* lead to large corresponding discontinuities in the calculated observables.

RESULTS

The results obtained using the modified potential for proton and neutron scattering by ^{27}Al, ^{56}Fe, and ^{208}Pb are now discussed. First, the results for ^{27}Al are shown in Figs. 3-8. In Fig. 3, experimental proton total reaction cross sections for ^{27}Al are compared with values calculated from the original potential of Schwandt *et al.*[3], for its energy range given by Eq. (1), and with values calculated from the modified potential, for its energy range given by Eq. (16). Although the experimental data are sparse, they clearly constrain the central absorptive potential of the modified potential to an energy dependence that is well approximated by a linear assumption above 140 MeV. Overall, the agreement with experiment is good. On the other hand, the third-order assumption of the original absorptive potential clearly leads to unphysical values of σ_R in the upper half of its energy range.

In Fig. 4, experimental neutron total cross sections for ^{27}Al are compared with values calculated from the original potential of Schwandt *et al.*[3], transformed to neutron scattering via Eqs. (17) and (18), and with values calculated from the modified potential, also transformed to neutron scattering via Eqs. (17) and (18) The energy ranges for the two potentials are, again,

given by Eqs. (1) and (16), respectively. The experimental neutron total cross sections constrain the central absorptive potential of the modified potential to an energy dependence that is, again, well approximated by a linear assumption above 140 MeV. Overall, the agreement with experiment is good, except in the region between approximately 100 and 200 MeV where the calculated values are 6-7% high -- possibly indicating deficiencies in the transformation given by Eqs. (17) and (18). Similar to the proton results, the third-order assumption of the original absorptive potential tends to produce unphysical values of σ_T in the upper third of its energy range.

In Figs. 5-8 the changes in the elastic scattering and analyzing power angular distributions that are caused by the modifications to the original potential are examined. For comparison purposes, it is assumed that the original potential predicts these experimental observables very well and therefore that a comparison of the predictions of the modified potential to those of the original potential is equivalent to comparisons with experiment. Energies that are 10 MeV below and above the boundary point of 140 MeV have been chosen to compare the elastic scattering in Figs. 5 and 6, and to compare the analyzing powers in Figs. 7 and 8. The elastic scattering hardly changes at all in Region I, for the entire angular range, and changes significantly in Region II only at angles above about 75° where it is approximately six orders of magnitude down from the forward scattering. Thus, the changes in the elastic scattering due to the modifications of the potential are small. The same conclusion is reached for the analyzing power, which hardly changes at all in Region I, and changes significantly in Region II only at angles above about 95.°

Results entirely similar to those just described for ^{27}Al are obtained for ^{56}Fe, shown in Figs. 9-14, and for ^{208}Pb, shown in Figs. 15-20. Note, however, that the experimental situation for the proton total reaction cross sections on ^{208}Pb, Fig. 15, is somewhat ambiguous and that the tendency toward diverging σ_R values calculated from the original potential is just beginning, near 180 MeV. Also note that in the case of the neutron total cross sections, the modified potential yields predictions that are within approximately 5% for ^{56}Fe, Fig. 10, and also approximately within 5% for ^{208}Pb, Fig. 16, except near 50 MeV where they are systematically low by as much as 10%. Finally, note that *no* angular dependent neutron data have been included in the analyses due to the sparsity of such data.

The conclusions of this section are that (1) the linear absorption of the modified potential provides for accurate calculation of the proton total reaction cross section for the extended energy range, (2) the transformation of the modified proton potential to the modified neutron potential via Eqs. (17) and (18) works reasonably well, 5-10%, over the same extended energy range, and (3) the modified potential does not overly deteriorate the predictive ability for elastic scattering and analyzing powers.

CONCLUSIONS

The overall conclusions from this preliminary work on obtaining a global medium-energy nucleon-nucleus phenomenological optical-model potential are that the present potential is of sufficient accuracy that *specific* neutron- and proton-induced reactions can be calculated with expectations that they sum to the correct physical values, and that simultaneously the angular-dependent proton elastic scattering observables are *reasonably* well reproduced, while the angular-dependent neutron elastic scattering observables *may* be reasonably well reproduced. Further work on this potential seems justified in light of the results obtained to date.

APPENDIX: COMPLEX PROJECTILES

Approximate medium-energy optical-model potentials for deuterons, ^{3}He, tritons, and alpha particles (d, h, t, α) can be obtained using a simplified Watanabe model.[7] Although no claims of high accuracy can be made with this approach, it has been found, nevertheless, to work

surprisingly well in producing starting parameter sets for optical-model searches on complex projectile scattering data. It has also been used with reasonable success to obtain complex projectile potentials where no data exists at all.

In simple form, one assumes that a proton-nucleus potential $V^p(E_p)$ and a neutron-nucleus potential $V^n(E_n)$ are given, where the geometries of the potentials are constant and the real and imaginary strengths are energy dependent, except for the spin-orbit strength, which is assumed to have the same constant value V_{SO} for both protons and neutrons. Then the simple version of the model states that the deuteron-nucleus potential is equal to the sum of the nucleon-nucleus potentials at half the energy, namely,

$$E_d = E_p/2 + E_n/2 \ ,$$

$$V^d(E_d) = V^p(E_p/2) + V^n(E_n/2) \ , \text{ and}$$

$$V^d_{SO} = V_{SO} \ .$$

Tensor polarization has been ignored in this approximation. Similarly, the helion-nucleus potential is equal to the sum of the nucleon-nucleus potentials at one-third the energy, namely,

$$E_h = E_p/3 + E_p/3 + E_n/3 \ ,$$

$$V^h(E_h) = V^p(E_p/3) + V^p(E_p/3) + V^n(E_n/3), \text{ and}$$

$$V^h_{SO} = V_{SO}/3 \ .$$

By the same logic, the triton-nucleus potential is given by

$$E_t = E_p/3 + E_n/3 + E_n/3 \ ,$$

$$V^t(E_t) = V^p(E_p/3) + V^n(E_n/3) + V^n(E_n/3), \text{ and}$$

$$V^t_{SO} = V_{SO}/3 \ .$$

Finally, the alpha-nucleus potential is equal to the sum of the nucleon-nucleus potentials at one-fourth the energy, namely,

$$E_\alpha = 2(E_p/4) + 2(E_n/4) \ , \text{ and}$$

$$V^\alpha(E_\alpha) = 2V^p(E_p/4) + 2V^n(E_n/4) \ .$$

Of course, in all cases the Coulomb potential is calculated appropriate to the charge of the complex projectile.

One would expect the model to perhaps work best for the deuteron, which is the least tightly bound of the four complex projectiles considered, and to perhaps work worst for the alpha particle, which is the most tightly bound of the four. At medium energies, however, the model performs reasonably well for alpha particle and ^{3}He scattering in addition to deuteron scattering. Note that an even simpler model can be used in this approach by replacing the neutron-nucleus potential $V^n(E_n)$ in the above equations with the proton-nucleus potential $V^p(E_p)$.

REFERENCES

1. D. G. Madland, Bull. Am. Phys. Soc. *31*, 1230 (1986).

2. D. G. Madland, Proc. IAEA Advisory Group Meeting on Nuclear Theory for Fast Neutron Data Evaluation, October 12-16, 1987, Beijing, Peoples Republic of China, to be published.

3. P. Schwandt *et al.*, Phys. Rev. C *26*, 55 (1982).

4. A. Nadasen *et al.*, Phys. Rev. C *23*, 1023 (1981).

5. F. G. Perey, Phys. Rev. *131*, 745 (1963).

6. P. Schwandt, Indiana University, private communication, May 1984.

7. S. Watanabe, Nucl. Phys. *8*, 484 (1958).

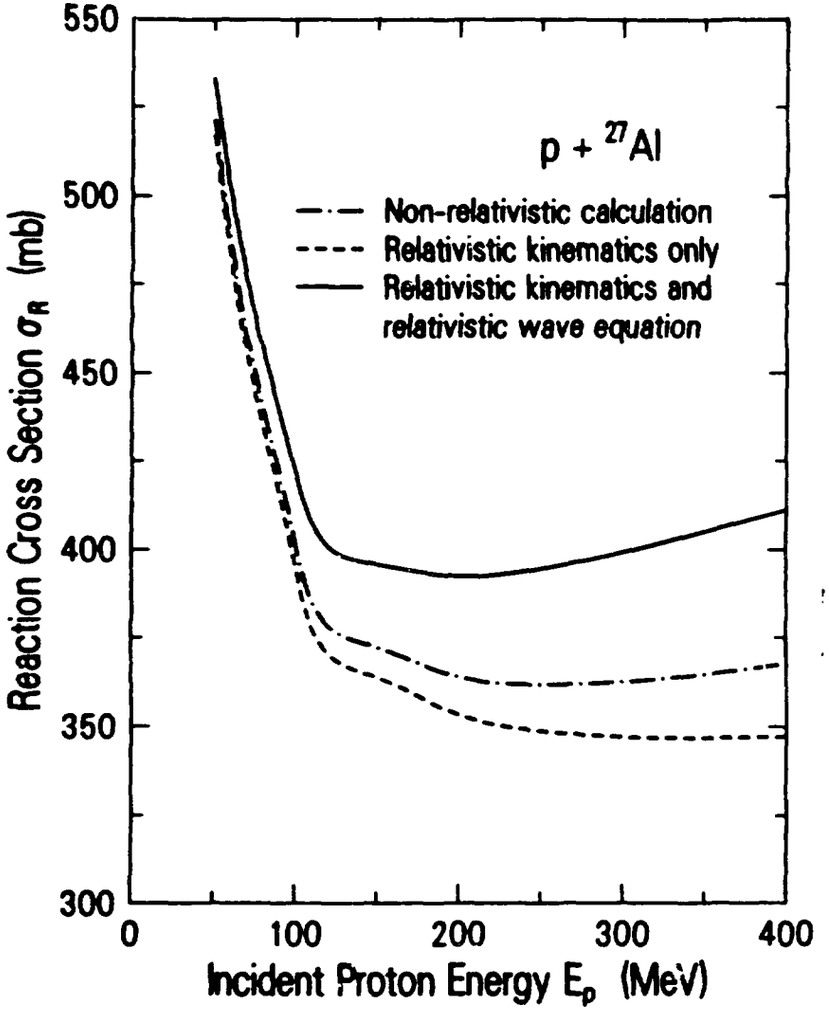

Fig. 1. Calculated proton total reaction cross section for three options on relativistic effects.

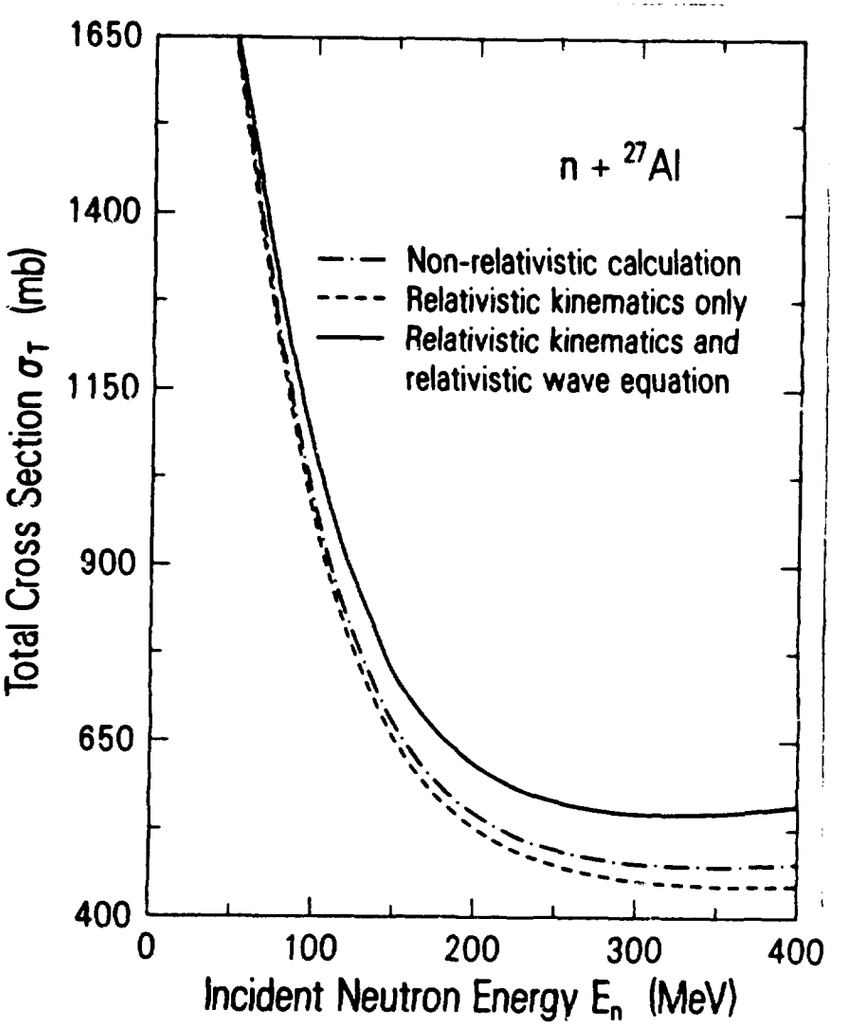

Fig. 2. Calculated neutron total cross section for three options on relativistic effects.

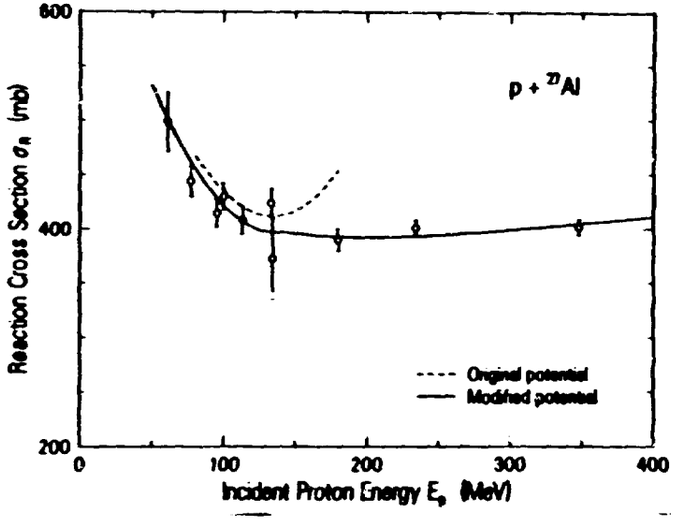

Fig. 3. Comparisons of measured and calculated proton total reaction cross sections for ^{27}Al.

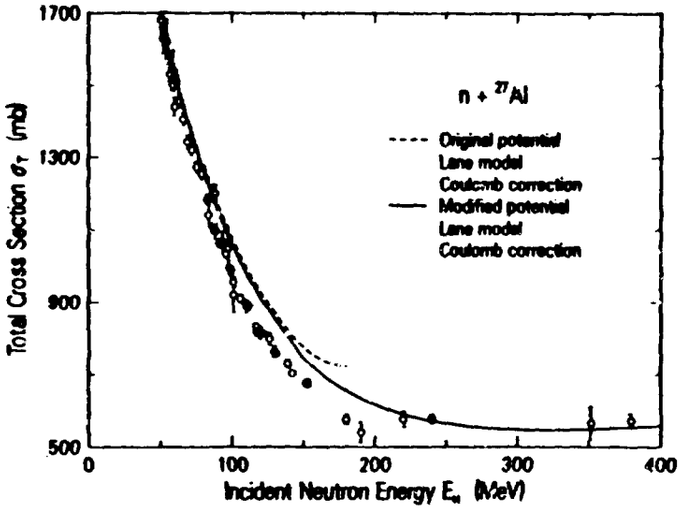

Fig. 4. Comparisons of measured and calculated neutron total cross sections for ^{27}Al.

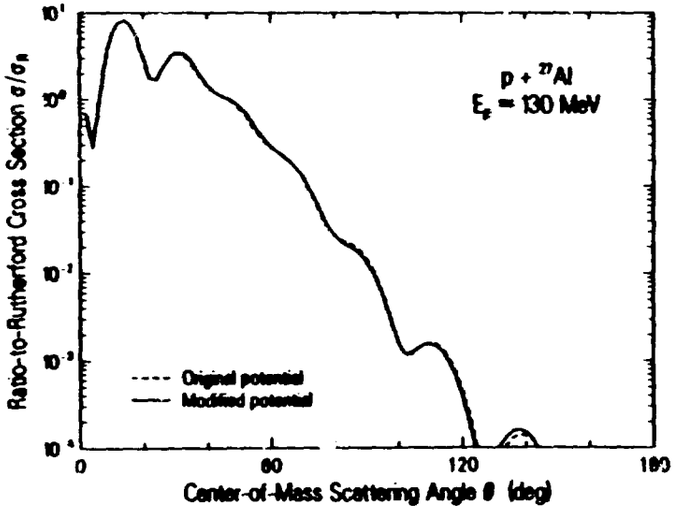

Fig. 5. Comparison of calculated elastic differential cross sections for the p + ^{27}Al reaction at 130 MeV (Region I).

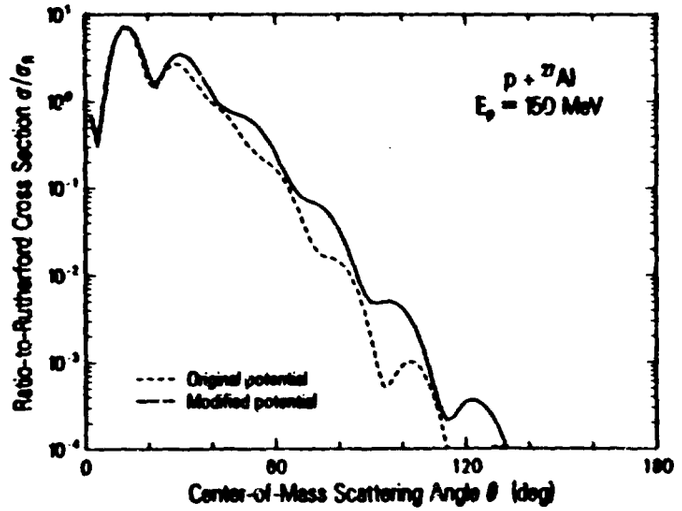

Fig. 6. Identical to Fig. 5 except at 150 MeV (Region II).

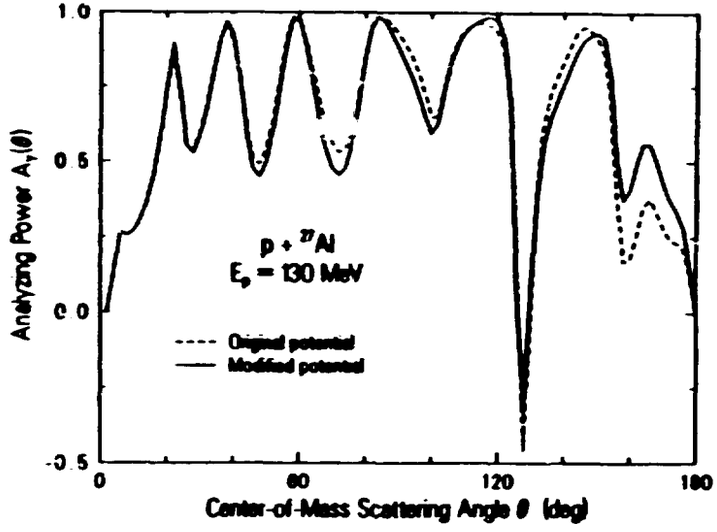

Fig. 7. Comparison of calculated analyzing powers for the p + ^{27}Al reaction at 130 MeV (Region I).

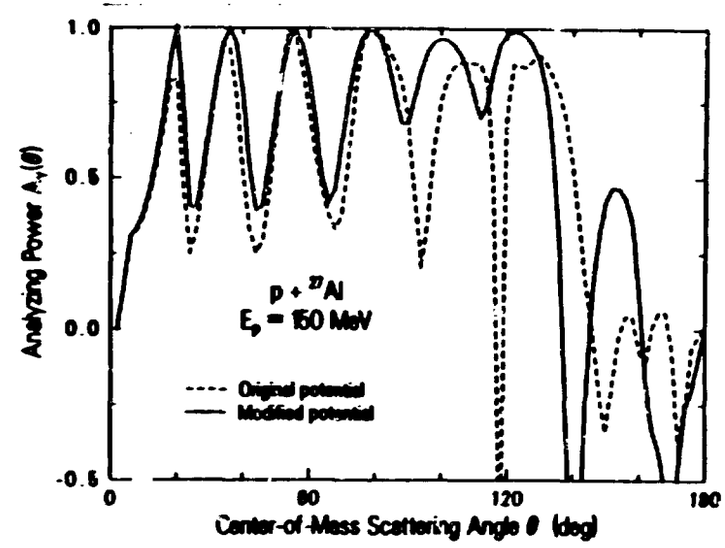

Fig. 8. Identical to Fig. 7 except at 150 MeV (Region II).

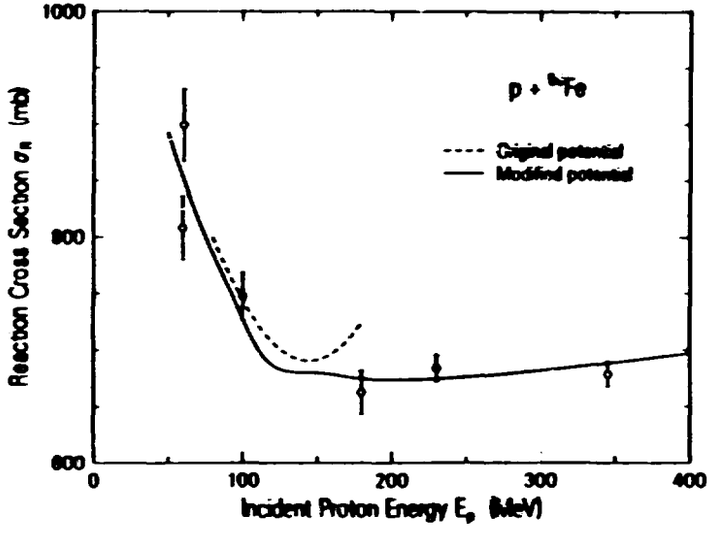

Fig. 9. Comparisons of measured and calculated proton total reaction cross sections for ^{56}Fe.

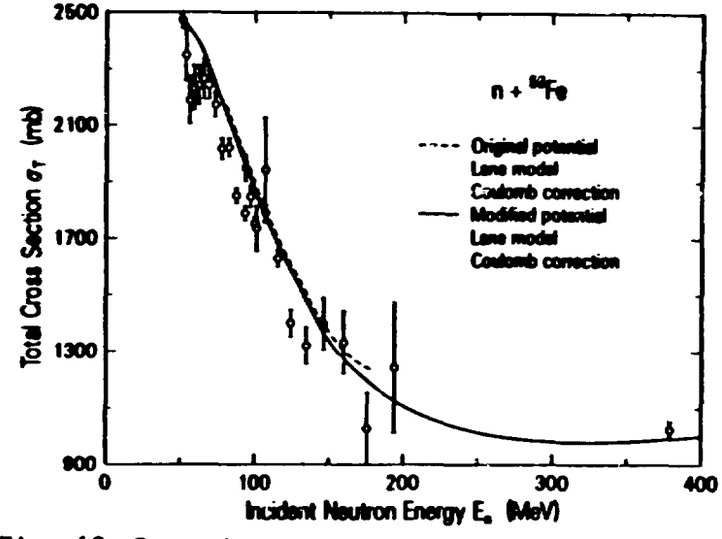

Fig. 10. Comparisons of measured and calculated neutron total cross sections for ^{56}Fe.

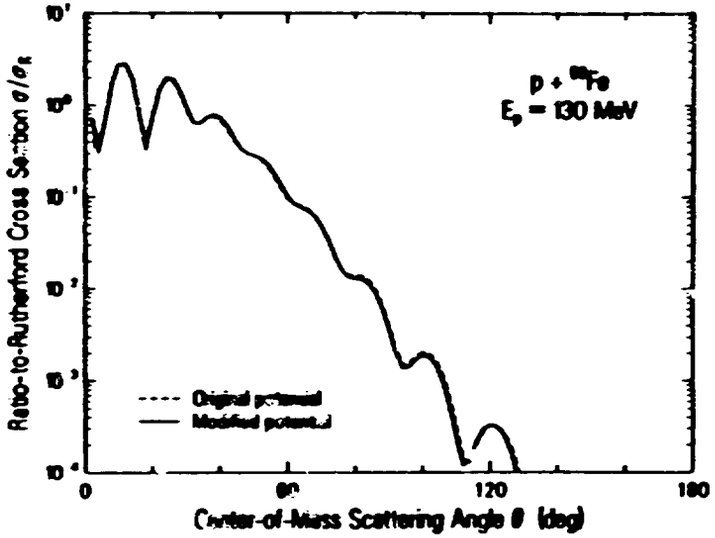

Fig. 11. Comparison of calculated elastic differential cross sections for the p + ^{56}Fe reaction at 130 MeV (Region I).

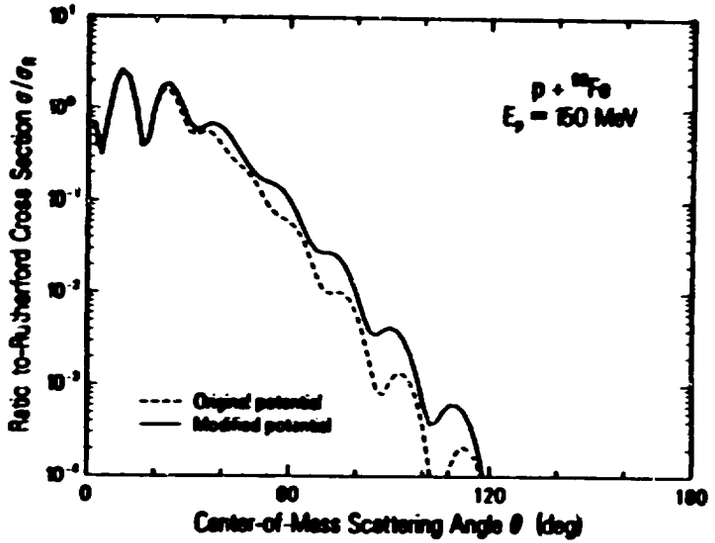

Fig. 12. Identical to Fig. 11 except at 150 MeV (Region II).

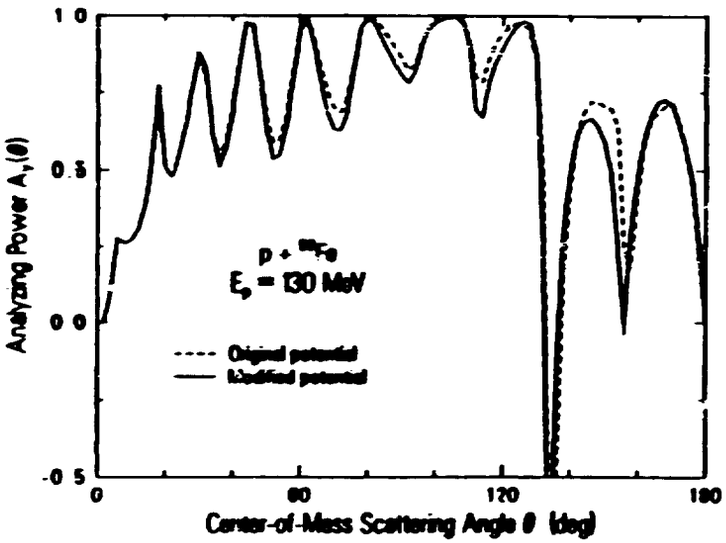

Fig. 13. Comparison of calculated analyzing powers for the p + ^{56}Fe reaction at 130 MeV (Region I).

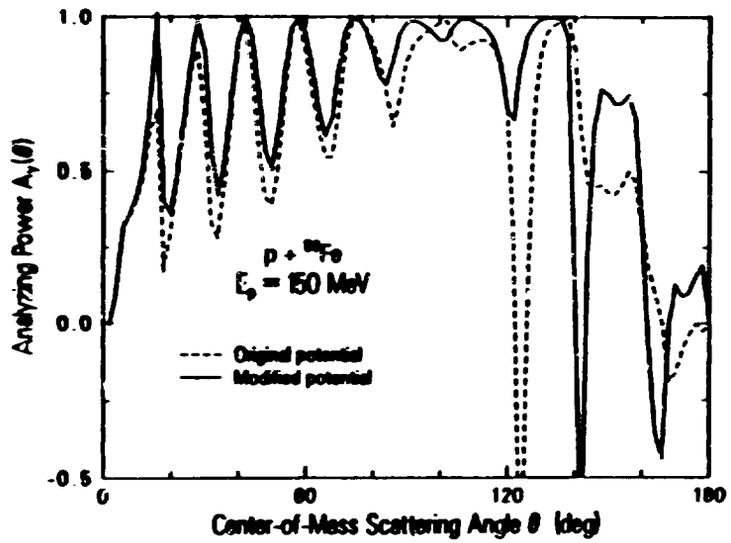

Fig. 14. Identical to Fig. 13 except at 150 MeV (Region II).

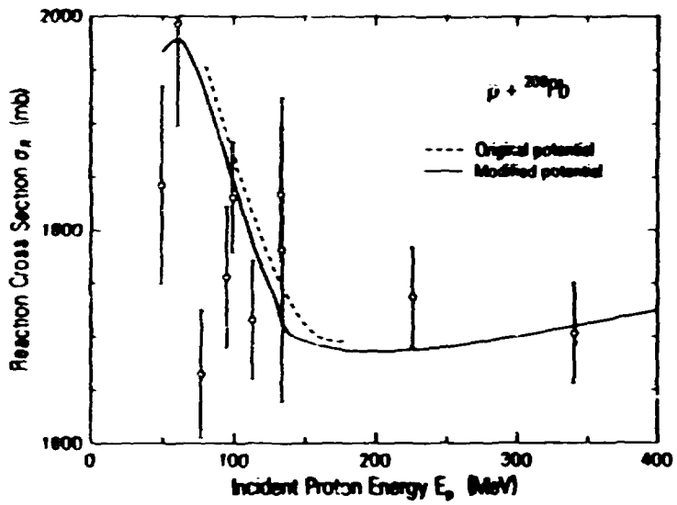

Fig. 15. Comparisons of measured and calculated proton total reaction cross sections for ^{208}Pb.

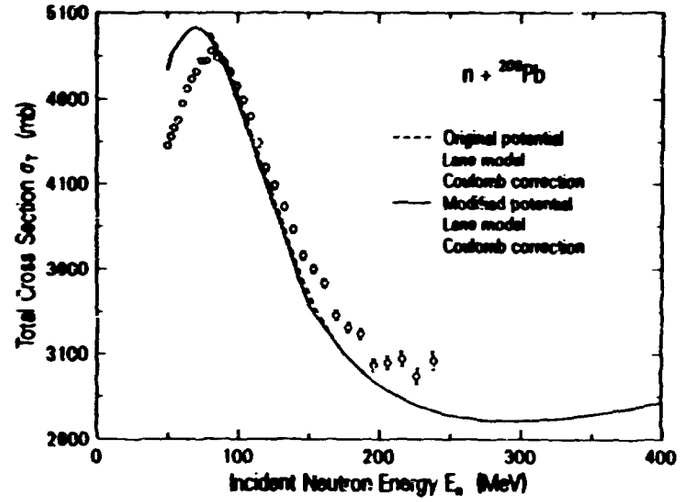

Fig. 16. Comparisons of measured and calculated neutron total cross sections for ^{208}Pb.

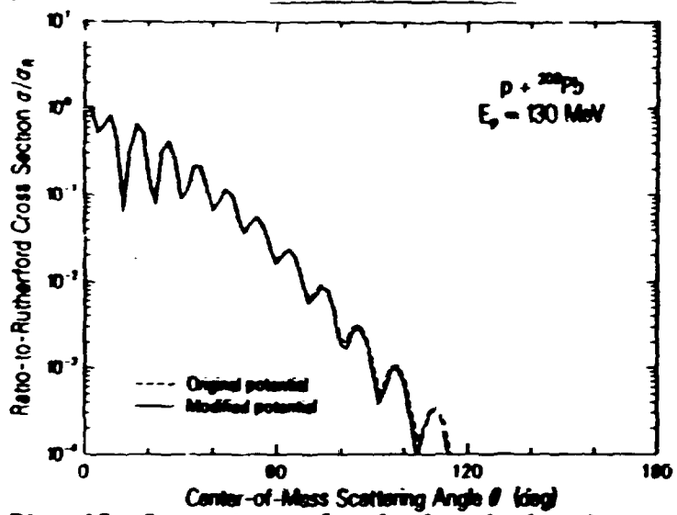

Fig. 17. Comparison of calculated elastic differential cross sections for the p + ^{208}Pb reaction at 130 MeV (Region I).

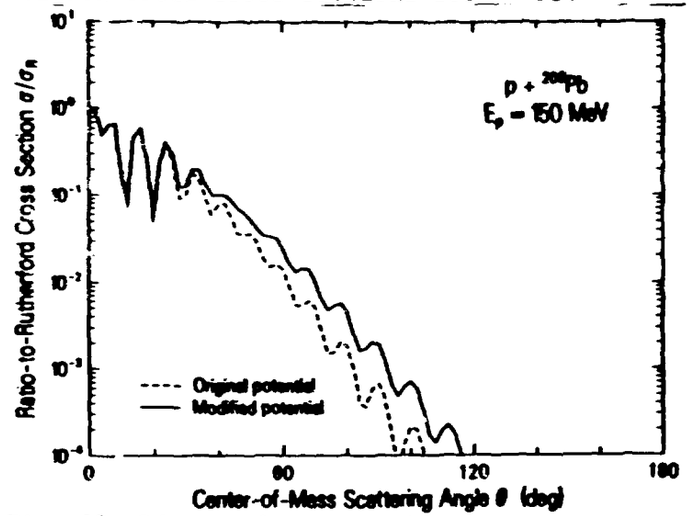

Fig. 18. Identical to Fig. 17 except at 150 MeV (Region II).

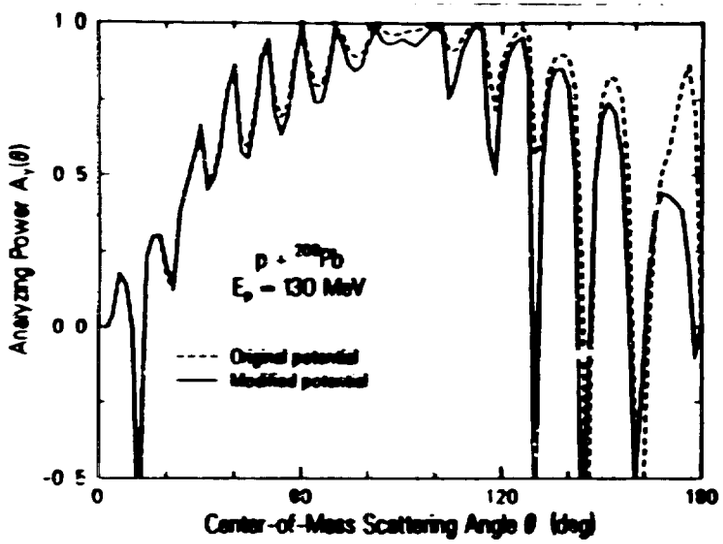

Fig. 19. Comparison of calculated analyzing powers for the p + ^{208}Pb reaction at 130 MeV (Region I).

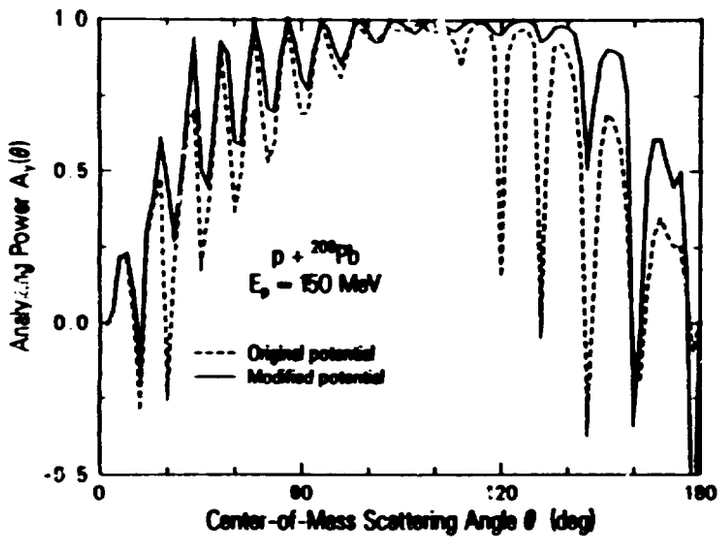

Fig. 20. Identical to Fig. 19 except at 150 MeV (Region II).